2024 23rd IEEE Intersociety Conference on Thermal and Thermomechanical Phenomena in Electronic Systems (ITherm) | 979-8-3503-6433-0/24/$31.00 ©2024 IEEE | DOI: 10.1109/ITherm55375.2024.10709548

Maximizing the Thermal Performance of Microheaters for Non-Volatile Phase Change Photonics: A Comparative Study of Pulse Width Parameter Effects

Francis Vasquez-Aza[1], Hongyi Sun[2,3], Chuanyu Lian[2,3], Yi-Siou Huang[2,3], Steven A. Vitale[4], Ichiro Takeuchi[2,5], Juejun Hu[6], Nathan Youngblood[7] Carlos A. Ríos Ocampo[2,3], Georges Pavlidis[1]

[1]*School of Mechanical, Aerospace, and Manufacturing Engineering, University of Connecticut, Storrs, CT 06269, USA*
[2]*Department of Materials Science and Engineering, University of Maryland, College Park, MD 20742, USA*
[3]*Institute for Research in Electronics and Applied Physics, University of Maryland, College Park, MD 20742, USA*
[4]*Advanced Materials and Microsystems Group, MIT Lincoln Laboratory, Lexington, MA 02139, USA*
[5]*Quantum Materials Center, Department of Physics, University of Maryland, College Park, MD 20742, USA*
[6]*Department of Materials & Science Engineering, Massachusetts Institute of Technology, Cambridge, MA 02139, USA*
[7]*Electrical & Computer Engineering Department, The University of Pittsburgh, Pittsburgh, PA 15213, USA*
georges.pavlidis@uconn.edu

***Abstract*—Guiding, manipulating, and detecting light is integral to modern photonic systems that can be designed for displays, memory, data transfer, and sensors. The prospect of realizing programmable yet zero-static power photonics has recently gained attention thanks to the rise of optical phase change materials (PCMs). PCMs have a unique set of properties that make them desirable for this task: nonvolatile retention and reversible switching between their amorphous and crystalline states, which, in addition, display distinct optical and electronic properties. Nonvolatile photonic devices have primarily relied on either electrical or optical switching of PCMs. Electrical switching offers effortless CMOS integration; however, it is predominantly limited to binary output. In contrast, optical switching enables accurate multilevel control but is limited in scalability. This paper studies an alternative electro-thermal approach to nonvolatile photonics by controlling the PCM phase via doped silicon microheaters. The results highlight the significance of precise spatial and temporal temperature control to ensure optimal modulation of the PCM. Specifically, this paper investigates the impact of the electric pulse width (0.2 µs to 10 µs) on the maximum temperature for two different microheater designs. High resolution (≈410 nm) transient thermoreflectance imaging (TTI) is used to measure and analyze the surface temperature distribution across each microheater under pulsed biasing. To assess the impact of varying pulse widths, this study systematically examines their effects on maximum temperature, response time, and maximum power. Shorter pulse widths (< 0.6 µs) enable higher currents, yet their impact on thermal response time can be limiting as the steady-state temperature is never reached. In contrast, longer pulse widths (> 1 µs) provide greater thermal stability but exhibit reduced maximum temperatures due to limited current levels. The experimental results demonstrate a nonlinear relationship between the peak temperature and the power supplied at sub-steady state thermalization time scales. For the specific microheater geometry, the optimal pulse width for achieving the highest temperature is found to be ≈ 0.4 µs.**

Keywords—Silicon, Microheaters, Thermoreflectance, Electric Pulse Width, Phase Change Material, Transient Thermal Dynamics

I. INTRODUCTION

The ever-increasing demand for high-performance photonic systems has led to an extensive exploration of novel approaches to improve the design and functionality of photonic integrated circuits [1]. Target applications for these devices range from optical signal processing [2], optical computing [3], displays [4], light detection [5] and quantum computing [6]. In recent times, nonvolatile switching has emerged as a promising avenue for photonics, with phase change materials (PCMs) standing out for their fast-switching times, long-term stability of the phase-states, high endurance cycles, and low energy consumption [7]. PCMs enable nonvolatile switching by having the ability to transition between amorphous and crystalline states rapidly and reversibly [8]. This property allows for the precise control of the optical transmission of PCMs.

The conventional methods of achieving nonvolatility in photonic devices have primarily revolved around electrical or optical switching [9]. While electrical switching offers seamless integration and scalability [10], it tends to have limited multi-level control. Multi-level control is the ability of a system to store and process information across numerous states, facilitating higher data density and more complex information processing [11]. It allows not only to control the level of data transmission (between 0 and 100%) but also to enable the storage and processing of information in more than two states, enabling emergent applications such as in-memory computing [12]. Achieving reliable multi-level operation with electrical control is challenging due to the stochastic nucleation of PCMs. This implies that only two states, complete amorphous or crystalline phase, can be consistently produced [13].

In contrast, when utilizing laser pulses, reliable multilevel operations can be accomplished via optical switching [14]. The PCM directly absorbs energy from pulses, generating a hotspot whose size can be deterministically controlled by tuning the width and power of the laser pulses, thus leading to reproducible spatial distributions of amorphous/crystalline domains, i.e. reliable multi-level response [15]. This process enables near-GHz, low-energy operations and, notably, a substantial number of multi-level states [13][15]. However, despite having the capability of deterministic multi-level control, optical switching faces challenges in scalability since routing optical pulses becomes difficult as the number of PCM elements increases [16].

Therefore, an alternative approach is needed to address the inherent tradeoff between scalability and multi-level control. This paper explores the feasibility of controlling PCMs photonics via external electro-thermal control by doped silicon microheaters. The temperature of the PCM determines its phase when either the crystallization or melting temperatures are achieved. Therefore, controlling the size and time-evolution of the microheaters thermal transition region (TTR) is crucial in enabling multilevel control [17]. Additionally, controlling the shape and the doping profile of silicon microheaters have the potential to spatially control the TTR, and thus, the PCM phase [18]. This paper aims to investigate the influence of electric pulse width on the maximum temperature for two different microheater designs, with a focus on the precise temperature control required for optimal modulation of PCMs. High-resolution Transient Thermoreflectance Imaging (TTI) [19] is employed to measure and analyze the surface temperature distribution across the microheaters during pulsed biasing. The study systematically examines the effects of varying pulse widths, ranging from 0.2 µs to 10 µs, on the peak temperature and maximum power. First, the maximum power dissipation (power rating) in each design was measured via high-speed electrical equipment. Subsequently, the peak temperature at the end of the pulse was measured.

II. Experimental Methods

A. Device Fabrication and Geometry

The microheaters were fabricated on 220-nm SOI wafers with ion-implanted phosphorous n+ ($\approx 4 \times 10^{18}$ cm^{-3}) and n++ ($\approx 10^{20}$ cm^{-3}) doped regions —the device fabrication is detailed in Ref [20]. A 100 nm-thick layer of aluminum was deposited onto the n++ regions to improve both the contact interface and electrical conductivity between microheaters and the electrical probes. The top view of the two microheaters' layout geometries is shown in Fig. 1.

Microheater 1 (M1) is comprised of three channels with identical dimensions, while Microheater 2 (M2) is characterized by a uniform surface area featuring a bow-tie geometry. Heat is generated within the doped areas of each microheater, with two contacts on the left and right sides utilized for applying voltage. The heat is generated through the Joule effect. The heat flux generation area for both microheaters is 90 µm² for M1 and 75 µm² for M2.

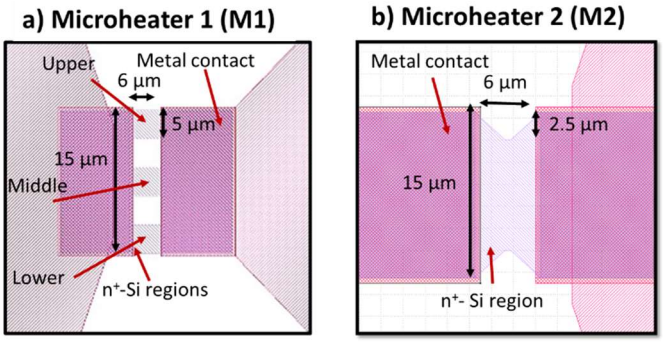

Fig. 1. Geometrical designs of two Silicon (Si) doped microheaters fabricated on a Silicon on insulator (SOI) wafer. In Microheater 1 (M1), the geometry is designed to generate heat across three channels whereas Microheater 2 (M2) is designed with a bow-tie geometry.

B. Electrical Testing

A pulsed IV system (Auriga AU5) was used to electrically bias the microheaters using between 5% - 20% duty cycle and pulse widths varying between 0.2-10 µs (specified in Table I). Initially, the microheaters were electrically biased, in 0.1 V increments, until breakdown was achieved for each respective pulse width. The maximum voltage and power at breakdown were determined when the device's current collapsed. The device's peak power (for long term operation) was then estimated to be ≈ 90% of the maximum power. This peak power was then used to measure the peak operating temperature associated with each respective pulse width. Due to small variations in breakdown voltages between devices, this power derating ensured that the temperature measured, for each pulse width, could be recorded on the same device without failure (ensuring a fair comparison of the thermal performance).

The Pulsed IV system was externally triggered by the TTI system in order to acquire thermal images at different time delays. An external oscilloscope (Tektronix 4 Series) was used to measure the delay between the device pulse rise and the trigger initiated from the TTI controller. The average delay was measured to be 128 ± 1.98 ns and was used to accurately synchronize the LED pulse delay in relation to the device pulse.

TABLE I. Electric Parameters Applied to TTI Equipment

Attempt	Pulse (µs)	Duty Cycle (%)	LED (ns)
1	0.2	5	50
2	0.3	7.5	50
3	0.4	10	50
4	0.5	12.5	50
5	0.6	15	50
6	0.8	20	60
7	1.0	20	60
8	1.5	20	62
9	2.0	20	75
10	5.0	20	150
11	10.0	20	350

The LED pulse delay determines the timing of the thermoreflectance measurement and represents the exact time that the temperature is recorded during the device pulse. Therefore, accurately quantifying the trigger delay time (specifically for device pulses < 0.5 µs) is an important

parameter for accurate synchronization of thermal imaging with the device pulse width. Additionally, the LED pulse width was methodically chosen to avoid any thermal images averaging over the voltage waveform edge. The settings for each temperature measurement are summarized in Table I.

C. *Transient Thermoreflectance Imaging (TTI)*

TTI was used to thermally characterize the microheaters' transient thermal dynamics [21], based on a lock-in CCD (Charge-coupled Device) approach. The thermoreflectance method measures changes in reflectivity due to a local temperature change. A single thermal image is captured by directing collimated light from a light emitting diode (LED) through an objective to illuminate the device and subsequently reflect back through the microscope to the CCD. The test setup is shown in Fig. 2 and additional details (including the LED timing configuration) can be found in [22]. When attempting to directly probe the reflectance of a semiconductor, the signal can be significantly improved by using excitation wavelengths near/above the bandgap of the semiconductor [24]. An illumination wavelength of 780 nm (1.59 eV) was therefore chosen due to the high reflectance obtained over the Silicon microheater region. Overall, the advanced lock-in averaging approach allows for simultaneous high spatial resolution (≈ 150 nm/pixel) and temporal resolution (≈ 50 ns) [23].

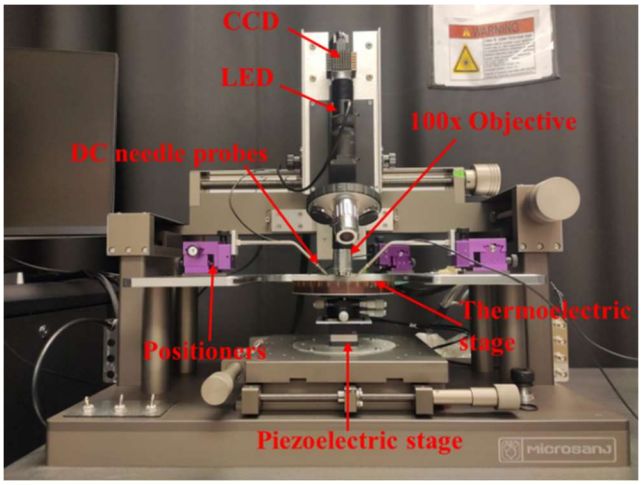

Fig. 2. Test setup includes the Light Emitting Diode (780 nm LED), the Charge Coupled Device (CCD), 100x Long Working Distance Objective, DC needle probes (with positioners) to make electrical contact, and piezoelectric/thermoelectric stage used for C_{TH} extraction and autofocusing.

Examples of thermal images acquired for each respective heater are shown in Fig. 3. The Regions of Interest (ROIs) for each microheater are indicated as black squares in Fig. 3. The selection of the regions was based on the maximum temperature region while covering a minimum number of 25 pixels. The accuracy of TTI relies on determining the thermoreflectance coefficient, C_{TH} (assuming a linear relationship between temperature rise and reflectance change). The C_{TH} of the top layer (silicon) was experimentally found using a 100× objective (NA = 0.7) and a temperature-controlled thermoelectric stage. The change in thermoreflectance (ΔR/R) was measured for a given set of temperature rises by increasing the stage temperature from 20 °C to 120 °C (in 20 °C steps). The surface temperature rise is independently measured with a thermocouple that is positioned near the microheater with thermal paste. Using an iterative approach (heating and cooling), the C_{TH} of the microheater region was monitored and calibrations were repeated until the C_{TH} value converged. For 780 nm excitation, the C_{TH} of the Silicon channel region was measured to be $(2.39 \pm 0.019) \times 10^{-4}$ K^{-1} for M1 and $(3.49 \pm 0.009) \times 10^{-4}$ K^{-1} for M2 (maps for each microheater are shown in Fig. 3). The uncertainty of the averaged C_{TH} was calculated using the standard error with 95% confidence intervals. The discrepancy in the C_{TH} between the two devices may be attributed to differences in the surface roughness and edge effects [21].

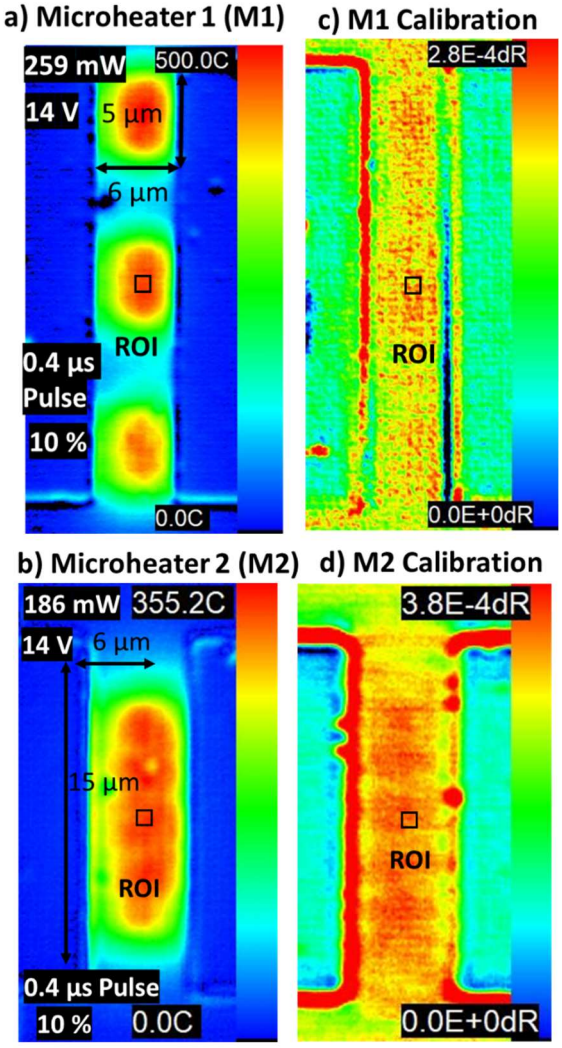

Fig. 3. Transient thermoreflectance images of a) Microheater 1 (M1) and b) Microheater 2 (M2) using a single thermoreflectance coefficient (C_{TH}). A 0.4 µs pulse width was applied under a 10% duty cycle. Temperature scale bar represents the temperature rise with reference to the stage temperature (20 °C). C_{TH} maps of c) M1 and d) M2. C_{TH} scale bar represents the reflectance change for a temperature rise of 100 °C. All images were captured using 780 nm LED.

An irregular heating profile was observed in M1 (Fig. 3a) that is comprised of three channels. It is expected that the upper (T_{upper}) and lower channel (T_{lower}) of M1 will reach similar temperature rises due to symmetry. By 'upper' and 'lower'

regions, it is referred to the doped areas situated at the top and bottom ends respectively, as shown in Fig. 1. Since the C_{TH} cross sectional profile obtained for M1 (Fig. 3c) reveals < 5% variation, the discrepancy (T_{upper}-$T_{lower} \approx 20$ K) suggests that the asymmetric Joule heating is caused by an uneven current distribution across the three channels.

III. Results and Discussion

A. Effect of Pulse Width on Peak Power

The peak power as a function of the pulse width is shown in Fig. 4. Two main regions are identified. For pulse widths longer than 2 µs, the peak power is independent of the pulse width, and this region is defined as the steady state power region. For pulse widths shorter than 2 µs, the peak power increases when decreasing the pulse width and this region is classified as the dynamic power region [25] [26]. The average peak power, under steady state, is measured to be 109 mW for M1 and 170 mW for M2. In the dynamic region, M1 exhibits a maximum peak power of 329.22 mW when applying a 0.2 µs pulse width. The maximum peak power measured in M2 was also obtained with a 0.2 µs pulse width, but the power was calculated to be 28% lower (259.22 mW). The increase in power for shorter pulses can be attributed to the increase in current that originates from reduced heat accumulation within the heater [26]. Compared to the steady state power obtained for M2, the peak power can be increased by 18 % when applying shorter pulses. The values of the maximum voltage, current and power measured as a function of the pulse width are displayed in Table II.

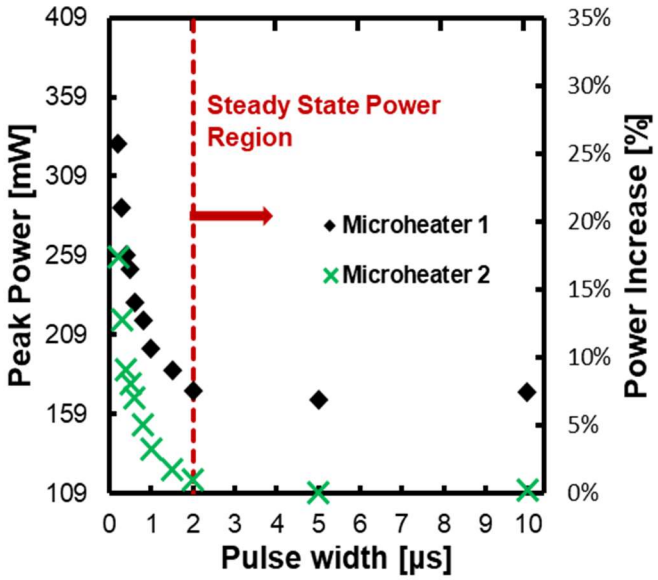

Fig. 4. Maximum electrical power as a function of pulse width. M1 is represented by diamond solid markers (black) and M2 is represented by crosses (green). The red dashed line is the minimum pulse width needed to enter the steady state power regime.

The maximum voltage reached before breakdown for each microheater was 15 V. However, M1 can reach higher current values (and thus higher power). The maximum current measured with a 0.2 µs pulse width is 21.60 mA and 17.25 mA for M1 and M2 respectively. For pulses longer than 2 µs, the current remains constant around 16.10 mA for M1 and 10.50 mA for M2. The larger current capability of M1 is attributed to the lower channel resistance of the heater with a smaller cross-sectional area (15 µm^2).

TABLE II. Electric Parameters Applied to TTI

	M1			M2		
Pulse Width (µs)	V (V)	I (mA)	P (mW)	V (V)	I (mA)	P (mW)
0.2	15.2	21.6	329.2	15.0	17.3	258.1
0.3	13.6	21.2	288.9	14.1	15.5	218.1
0.4	12.9	20.2	259.6	13.3	14.1	186.9
0.5	12.4	20.3	250.3	12.4	14.4	177.6
0.6	12.4	18.5	229.0	12.5	13.6	169.3
0.8	11.7	18.7	218.3	11.5	13.2	151.9
1.0	11.4	17.6	200.4	11.6	11.7	136.4
1.5	10.9	17.1	186.8	11.1	11.1	123.5
2.0	10.4	16.7	173.6	10.7	10.9	117.1
5.0	10.5	16.1	168.2	10.4	10.5	109.3
10.0	10.7	16.2	172.6	10.5	10.6	110.8

B. Thermal characterization

Assuming the measured C_{TH} values have a linear relationship [21], the transient surface temperature rise of the Silicon active channel can be estimated (Fig. 5).

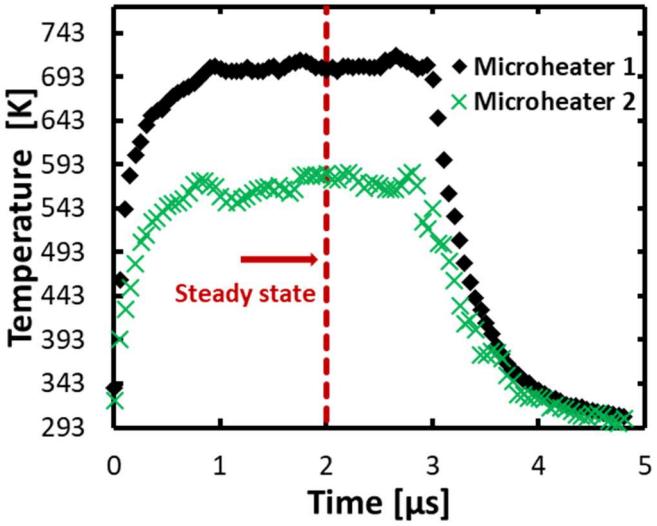

Fig. 5. Transient temperature profiles applying a 9.5 V pulse with a 30% duty cycle. Averaged temperatures, extracted from the ROIs shown in Fig. 3, were acquired with 50 ns time steps. M1 is represented by solid black diamonds and M2 by green crosses. A red dashed line indicates the electrical steady state power region which is derived from Fig. 4.

Prior to quantifying the peak temperature for different pulse widths, a full transient sweep was performed to understand the heaters' dynamic thermal behavior and extract their respective thermal time constants. A 3 µs long pulse under a 30% duty cycle was applied to both heaters. Due to the lower channel resistance of M1, a 9.23 V bias resulted in M1 exhibiting a 50% higher peak power dissipation (139.8 mW vs 93.5 mW). A 50 ns LED pulse (minimum pulse width) was used to obtain a transient profile with the system's highest temporal resolution. In comparison to the steady state power condition, the steady state temperature is reached significantly earlier than 2 µs for both microheaters. The heating thermal time constants (time required to reach 63.2 % of the steady state temperature) are 0.15 µs (M1)

and 0.20 µs (M2). The absolute peak temperature measured at end of the pulse (t = 3 µs) was measured to be (705.15 ± 1.63) K and (567.15 ± 4.12) K for M1 and M2 respectively. When numerically compared as temperature rise values, the 50% increase in temperature is directly proportional to the increase in power dissipation. The uncertainty associated with the temperature was calculated based on the total propagated uncertainty (including the C_{TH} and the reflectance change).

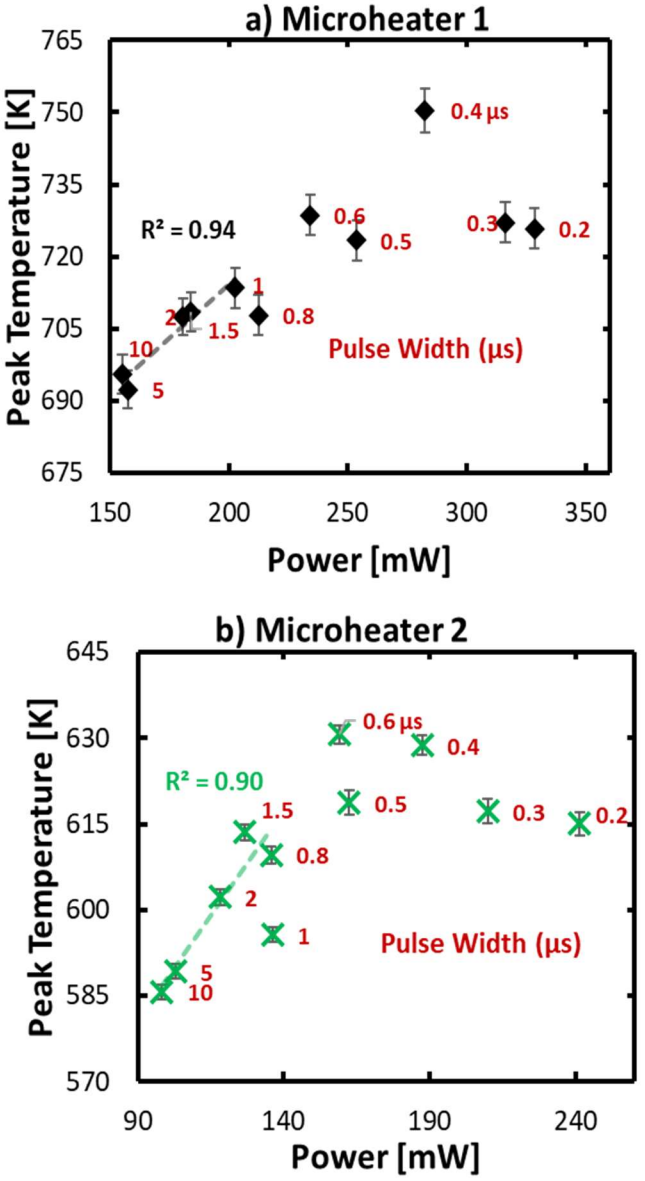

Fig. 6. Absolute peak temperature as a function of pulse width. The maximum peak temperature against peak power for different pulse widths are shown for a) M1 (solid black diamonds) and b) M2 (green crosses). A linear regression was applied to demonstrate the relationship between temperature and power in the electrical steady state region. The pulse widths (µs) are labeled in red.

After determining the thermal time constants, the peak temperature was measured for different pulse widths (at the end of the pulse as described in Table I). The temperature rise was extracted from the ROIs shown in Fig. 3. Fig. 6a depicts the peak temperature for M1, where the y-axis represents the absolute temperature (K), and the x-axis shows the peak power (which was derated by 5-10% for long term operation). The pulse width for each marker is labeled in red to highlight the dependence of the pulse width on temperature. For M1, the peak temperature, (750.35 ± 4.51) K was obtained when applying a 0.4 µs pulse. In contrast, the minimum peak temperature, (692.32 ± 3.90) K, was observed when applying a 5-10 µs pulse.

For M1, the expected linear relationship for temperature vs. power is observed for pulse widths between 0.4 µs and 10 µs (Fig. 6a). This will be considered the steady state thermal region in which the pulse width is reduced, the power dissipated increases, and a proportionally higher temperature is achieved. When shortening the pulse width < 0.4 µs, the power dissipated continues to increase, however, the peak temperature begins to decrease. This can possibly be related to the thermal time constant extracted for M1 from Fig. 5 (0.15 µs). For pulse widths < 0.4 µs, the microheaters have not reached full dynamic thermal equilibrium which can translate to lower temperatures despite an increase in power dissipation. The peak temperature measured at 0.8 µs is shown to be an outlier and can possibly be explained by some discrepancies in the power applied or vibrations during the attempt.

A similar behavior is observed for M2 and is depicted in Fig. 6b. In the electrical steady state power region (pulse width > 2 µs), the temperature and peak power show a linear relationship. However, some discrepancies are identified when measuring the temperature rises for the 0.5 µs, 0.8 µs and 1 µs pulse widths. These pulses exhibit a lower temperature rise (≈ 10 K decrease) in contrast to the temperatures obtained for the 0.6 µs and 0.4 µs pulse widths. The underestimation can be explained due to anomalous asynchronization between the device trigger and the LED delay time (the time at which the temperature is acquired). The CCD averages thousands of images at a given LED time delay. A small shift in the LED time delay (ns) could offset the time position when the temperature is measured into the cooling region (i.e. when the pulse is off). The peak temperature in M2 is found near 0.4 µs and 0.6 µs pulse widths (≈ 630 K). The minimum peak temperature is measured to be (585.62 ± 1.33) K for a 10 µs pulse. This difference in temperature represents 17% higher values when short pulses (0.6 µs) are applied.

IV. Conclusions

This research demonstrates the significant impact of electrical pulse width on the maximum temperature/power of two different microheaters designs. Within the preliminary segment of the study, two discrete domains, the steady state, and the dynamic power region, are identified based on pulse width duration. For pulse widths longer than 2 µs (steady state power region), the peak power is found to be independent of the pulse width. For pulse widths shorter than 2 µs (dynamic power region), the peak power increases as the pulse width decreases. Then, the specific peak power values were measured for both microheater designs exhibiting different power characteristics in function of the pulse width. Additionally, this research provides insights into the maximum voltage and current values achieved for each microheater design, highlighting the distinct current capabilities of the two designs.

The second segment studies the impact of pulse width on the thermal response and the maximum temperature. The thermal time constants were determined, with M1 exhibiting a faster thermal response compared to M2 (0.15 µs vs 0.2 µs). The temperature profiles revealed that the microheaters reached steady state temperatures significantly earlier than 2 µs. The main difference between the microheaters could be attributed to a more efficient heat dissipation of M1 due to the geometric characteristics or a larger heating area (90 μm^2). The results demonstrate the impact of the pulse width on the peak temperature and power dissipation. A linear relationship between temperature and power dissipation was observed for pulse widths longer than 2 µs (electrical steady-state region). However, for pulse widths shorter than 2 µs, the peak temperature exhibited a nonlinear response, with a decrease in temperature observed for pulse widths below 0.4 µs. This behavior is attributed to the microheaters not reaching dynamic thermal equilibrium for very short pulses. Interestingly, our results explain the empirically found optimal 0.4 µs amorphization pulse using the Microheater 2 geometry to switch Sb_2Se_3 in Ref. [20] considering also that the amorphization of this PCM requires melting over 600°C and quenching. Finally, these findings offer valuable information for understanding the power dynamics and current capabilities of the two microheater designs, providing essential knowledge for the development of efficient and reliable temperature modulation strategies in nonvolatile photonic applications.

ACKNOWLEDGMENT

C.R.O. acknowledges support from the U.S. National Science Foundation under Grant ECCS-2210168 and the Minta Martin Foundation through the University of Maryland.

REFERENCES

[1] W. Bogaerts *et al.*, "Programmable photonic circuits," *Nature*, vol. 586, no. 7828, pp. 207–216, 2020, doi: 10.1038/s41586-020-2764-0.

[2] A. Macho-Ortiz, D. Pérez-López, and J. Capmany, "Optical Implementation of 2 × 2 Universal Unitary Matrix Transformations," *Laser Photon Rev*, vol. 15, no. 7, p. 2000473, Jul. 2021, doi: https://doi.org/10.1002/lpor.202000473.

[3] C. Wu, H. Yu, S. Lee, R. Peng, I. Takeuchi, and M. Li, "Programmable phase-change metasurfaces on waveguides for multimode photonic convolutional neural network," *Nat Commun*, vol. 12, no. 1, p. 96, 2021, doi: 10.1038/s41467-020-20365-z.

[4] N. Collings, A. Davey, J. Christmas, D. Chu, and B. Crossland, "The Applications and Technology of Phase-Only Liquid Crystal on Silicon Devices," *Journal of Display Technology*, vol. 7, pp. 112–119, Mar. 2011, doi: 10.1109/JDT.2010.2049337.

[5] X. Zhang, K. Kwon, J. Henriksson, J. Luo, and M. C. Wu, "A large-scale microelectromechanical-systems-based silicon photonics LiDAR," *Nature*, vol. 603, no. 7900, pp. 253–258, 2022, doi: 10.1038/s41586-022-04415-8.

[6] N. C. Harris *et al.*, "Quantum transport simulations in a programmable nanophotonic processor," *Nat Photonics*, vol. 11, no. 7, pp. 447–452, 2017, doi: 10.1038/nphoton.2017.95.

[7] J. Feldmann *et al.*, "All-optical signal processing using phase-change nanophotonics," in *2017 19th International Conference on Transparent Optical Networks (ICTON)*, 2017, pp. 1–3. doi: 10.1109/ICTON.2017.8024746.

[8] P. Prabhathan *et al.*, "Roadmap for phase change materials in photonics and beyond," *iScience*, vol. 26, no. 10, p. 107946, 2023, doi: https://doi.org/10.1016/j.isci.2023.107946.

[1]

[9] Z. Fang, R. Chen, B. Tossoun, S. Cheung, D. Liang, and A. Majumdar, "Non-volatile materials for programmable photonics," *APL Mater*, vol. 11, no. 10, 2023, doi: 10.1063/5.0165309.

[10] R. Chen, Z. Fang, F. Miller, H. Rarick, J. E. Fröch, and A. Majumdar, "Opportunities and Challenges for Large-Scale Phase-Change Material Integrated Electro-Photonics," *ACS Photonics*, vol. 9, no. 10, pp. 3181–3195, Oct. 2022, doi: 10.1021/acsphotonics.2c00976.

[11] Y. Wang, J. Ning, L. Lu, M. Bosman, and R. E. Simpson, "A scheme for simulating multi-level phase change photonics materials," *NPJ Comput Mater*, vol. 7, no. 1, p. 183, 2021, doi: 10.1038/s41524-021-00655-w.

[12] S. Sciara *et al.*, "Scalable and effective multi-level entangled photon states: a promising tool to boost quantum technologies," vol. 10, no. 18, pp. 4447–4465, 2021, doi: doi:10.1515/nanoph-2021-0510.

[13] C.-Y. Lee *et al.*, "Spatial and temporal control of glassy-crystalline domains in optical phase change materials," *Journal of the American Ceramic Society*, vol. 107, no. 3, pp. 1543–1556, Mar. 2024, doi: https://doi.org/10.1111/jace.19541.

[14] Z. Cheng, C. Ríos, W. H. P. Pernice, C. D. Wright, and H. Bhaskaran, "On-chip photonic synapse," *Sci Adv*, vol. 3, no. 9, p. e1700160, Dec. 2023, doi: 10.1126/sciadv.1700160.

[15] C. Rios *et al.*, "Controlled switching of phase-change materials by evanescent-field coupling in integrated photonics [Invited]," *Opt Mater Express*, vol. 8, no. 9, pp. 2455–2470, 2018, doi: 10.1364/OME.8.002455.

[16] A. Shafiee, S. Pasricha, and M. Nikdast, "A Survey on Optical Phase-Change Memory: The Promise and Challenges," *IEEE Access*, vol. 11, pp. 11781–11803, 2023, doi: 10.1109/ACCESS.2023.3241146.

[17] P. Prabhathan *et al.*, "Roadmap for phase change materials in photonics and beyond," *iScience*, vol. 26, no. 10. Elsevier Inc., Oct. 20, 2023. doi: 10.1016/j.isci.2023.107946.

[18] Z. Fang, R. Chen, J. Zheng, and A. Majumdar, "Non-Volatile Reconfigurable Silicon Photonics Based on Phase-Change Materials," *IEEE Journal of Selected Topics in Quantum Electronics*, vol. 28, no. 3: Hybrid Integration for Silicon Photonics, pp. 1–17, 2022, doi: 10.1109/JSTQE.2021.3120713.

[19] M. Farzaneh *et al.*, "CCD-based thermoreflectance microscopy: principles and applications," *J Phys D Appl Phys*, vol. 42, no. 14, p. 143001, 2009, doi: 10.1088/0022-3727/42/14/143001.

[20] C. Ríos *et al.*, "Ultra-compact nonvolatile phase shifter based on electrically reprogrammable transparent phase change materials," *PhotoniX*, vol. 3, no. 1, p. 26, 2022, doi: 10.1186/s43074-022-00070-4.

[21] M. Farzaneh *et al.*, "CCD-based thermoreflectance microscopy: principles and applications," *J Phys D Appl Phys*, vol. 42, no. 14, p. 143001, 2009, doi: 10.1088/0022-3727/42/14/143001.

[22] S. Sandell, E. Chávez-Ángel, A. El Sachat, J. He, C. M. Sotomayor Torres, and J. Maire, "Thermoreflectance techniques and Raman thermometry for thermal property characterization of nanostructures," *J Appl Phys*, vol. 128, no. 13, 2020, doi: 10.1063/5.0020239.

[23] G. Pavlidis, D. Kendig, L. Yates, and S. Graham, "Improving the Transient Thermal Characterization of GaN HEMTs," in *2018 17th IEEE Intersociety Conference on Thermal and Thermomechanical Phenomena in Electronic Systems (ITherm)*, 2018, pp. 208–213. doi: 10.1109/ITHERM.2018.8419649.

[24] K. Maize *et al.*, "High Resolution Thermal Characterization and Simulation of Power AlGaN/GaN HEMTs Using Micro-Raman Thermography and 800 Picosecond Transient Thermoreflectance Imaging," in *2014 IEEE Compound Semiconductor Integrated Circuit Symposium (CSICS)*, 2014, pp. 1–8. doi: 10.1109/CSICS.2014.6978561.

[25] X. Xie, K. Li, Q. Li, A. Beling, and J. C. Campbell, "Photonic generation of high-power pulsed microwave signals with peak powers up to 14.2 Watt," in *2015 Conference on Lasers and Electro-Optics (CLEO)*, 2015, pp. 1–2.

[26] K. Sasahira, K. Kuroda, and Y. Yoshikuni, "Pulse amplification characteristics of a CW pumped Erbium-Doped Fiber Amplifier," in *OECC 2010 Technical Digest*, 2010, pp. 346–347.